JOURNAL OF SYNCHROTRON RADIATION

ISSN 1600-5775

A high-temperature furnace for multimodal synchrotron-based X-ray microscopy and diffraction imaging

Louis Lesage,[a] Yves Watier,[a] Helena Isern,[a] Aditya Shukla,[a] Virginia Sanna,[a] Thomas Dufrane,[a] Yubin Zhang,[b] Carsten Detlefs[a] and Can Yıldırım[a]*

[a]Experiments Division, European Synchrotron Radiation Facility, 71 Avenue des Martyrs, CS40220, 38043 Grenoble Cedex 9, France, and [b]Department of Civil and Mechanical Engineering, Technical University of Denmark, 2800 Kgs Lyngby, Denmark. *Correspondence e-mail: can.yildirim@esrf.fr

Received 9 July 2025
Accepted 14 November 2025

Edited by M. Guizar-Sicairos, Paul Scherrer Institute, Switzerland, and EPFL, Switzerland

Keywords: furnaces; X-ray diffraction; synchrotrons; dark-field X-ray microscopy; X-ray imaging; grain growth.

The design, calibration and initial application of a non-contact high-temperature furnace developed for *in situ* synchrotron X-ray experiments are presented. The system enables a stable operation up to 1000°C, with heating rates exceeding 6000°C min^{-1} and thermal stability better than ±2°C. Temperature calibration was performed using (i) direct measurements with a thermocouple to characterize heating and cooling ramp rates and map temperature gradients along the *x*, *y* and *z* axes; and (ii) synchrotron X-ray diffraction to track the ferrite-to-austenite (body-centered cubic to face-centered cubic) phase transition in an iron grain under beamline conditions. The furnace's contactless geometry provides full translational and rotational freedom, with 360° rotation and wide tilt capabilities, making it fully compatible with a range of diffraction and imaging techniques. Its 3D-printed modular body includes closable apertures for auxiliary functions such as active cooling or X-ray fluorescence. The design is easily customizable for diverse experimental requirements and can be adapted to most beamlines. The furnace has been implemented at the ID03 beamline of the European Synchrotron Radiation Facility (ESRF), which supports dark-field X-ray microscopy (DFXM), 3D X-ray diffraction, magnified topotomography, phase-contrast tomography and diffraction contrast tomography. As a first application, a DFXM case study on a cold-rolled Al1050 sample during isothermal annealing is presented. The imaging of a selected grain before and after the heat treatment reveals strain relaxation and grain growth. This furnace offers a robust and flexible platform for high-temperature synchrotron studies across materials science, including metals, ceramics and energy materials. It is now part of the ESRF sample environment pool and is available to all users.

1. Introduction

The microstructure of a material plays a key role in determining its macroscopic properties and performance in engineering applications. Heat treatments are widely used across industries to tailor these microstructures, thereby tuning mechanical properties such as strength, ductility and hardness. To better understand how thermal stimuli drive changes in microstructures, *in situ* and *operando* studies with sufficient spatial and temporal resolution are essential.

Synchrotron-based X-ray techniques have emerged as powerful non-destructive tools for investigating such transformations over multiple length scales. Traditional methods, such as scanning electron microscopy with electron backscatter diffraction and transmission electron microscopy, provide excellent spatial resolution but are limited to surface or thin foil analysis and often require invasive sample preparation. In contrast, synchrotron diffraction imaging

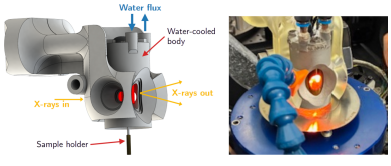

methods such as three-dimensional X-ray diffraction (3DXRD) (Poulsen, 2004), diffraction contrast tomography (DCT) (Reischig *et al.*, 2013), phase-contrast tomography (Cloetens *et al.*, 1997) and topography (Lang, 1993; Yildirim *et al.*, 2021) offer non-destructive three-dimensional insight into the internal structure of polycrystalline materials. Among these methods, dark-field X-ray microscopy (DFXM) has emerged as a powerful technique for high-resolution imaging of orientation and strain within individual grains embedded in bulk crystalline materials, achieved by placing an objective lens in the diffracted beam path (Simons *et al.*, 2015; Yildirim *et al.*, 2020*a*). Following the Extremely Brilliant Source upgrade (Cloetens *et al.*, 2025) of the European Synchrotron Radiation Facility (ESRF), the ID03 beamline (Isern *et al.*, 2025) was constructed to host the DFXM technique in conjunction with complementary techniques, including 3DXRD, DCT, diffraction tomography, X-ray topography and phase-contrast tomography, thereby enabling comprehensive multimodal and multiscale investigations of crystalline materials.

The development of advanced imaging techniques has been accompanied by a growing interest in studying sample behavior under non-ambient conditions, leading to the need for devices capable of simulating real sample processing or in-service environments. Such devices often require original designs to ensure compatibility with the beamline setup while avoiding obstruction of the X-ray beam. Environmental modifications may include controlling the gas environment around the sample at varying pressures, using high-pressure or high-vacuum cells (Van Rijn *et al.*, 2010), or regulating humidity levels (Derome *et al.*, 2011; Nopens *et al.*, 2025). Temperature control can also be achieved, either by employing cryostreams (Mitchell & Garman, 1994; Snell *et al.*, 2007) or cryostats (Martínez-Criado *et al.*, 2007; Hirao *et al.*, 2020) for low-temperature conditions or by employing lasers (Fife *et al.*, 2012; Hirao *et al.*, 2020) and furnaces (Buras *et al.*, 1984; Puig-Molina *et al.*, 2001) for high-temperature environments, potentially under controlled atmosphere (Bellet *et al.*, 2003; Holler *et al.*, 2022). Such developments have supported the growing interest over the last decade in studying the microstructural evolution of crystalline materials under external thermal stimuli using advanced synchrotron imaging techniques (Yildirim *et al.*, 2022, 2025; Ahl *et al.*, 2020; Dresselhaus-Marais *et al.*, 2021; Mavrikakis *et al.*, 2019).

A previous furnace developed for the ID06 beamline, where DFXM experiments were previously conducted, is no longer compatible with other goniometer setups and faced several technical limitations (Yildirim *et al.*, 2020*b*; Kutsal *et al.*, 2019). Notably, the furnace had a restricted tilt range and narrow angular apertures for the X-ray beam, both of which are critical for aligning grains to meet diffraction conditions. Although it offered excellent temperature stability, the sample was offset from the goniometer's center of rotation in certain directions, further limiting its suitability for DFXM, where precise angular alignment is essential. An alternative heating approach involved the use of a gas blower (Yildirim *et al.*, 2022, 2025); however, it lacked the stability required for achieving nanometre-scale resolution. During DFXM experiments, detector images often failed to stabilize, most likely due to uneven heating caused by inconsistent gas flow. Additionally, the exhausted hot gas typically heats up the goniometer stage or surrounding structural frames, further destabilizing the system. The gas flow might also have contributed directly to unintended sample movement. To compound these issues, gas blowers are costly and offer limited temperature control, making experiments difficult to reproduce. To address these limitations and support the advancement of synchrotron techniques toward *operando* and high-throughput studies, a heating solution compatible with the ID03 sample goniometer (Isern *et al.*, 2025) is needed, one that combines thermal precision, mechanical flexibility and experimental reproducibility.

Here, we present a newly developed non-contact furnace that enables full 360° sample rotation and a wide tilt range, ensuring seamless integration with advanced goniometer setups. Its 3D printed body enables customization for adaptation to various beamlines and characterization techniques. We report on the furnace's thermal performance, including its temperature homogeneity and ramp rates, based on *in situ* thermocouple measurements. In addition, we demonstrate how the absolute temperature at the sample position can be determined by monitoring phase transformations and lattice parameter evolution in reference samples. Finally, we showcase the capabilities of the system for *in situ* studies by capturing grain growth in an aluminium alloy during annealing using DFXM.

2. Description of the furnace

2.1. Conception of the furnace

Fig. 1 shows computer-aided design (CAD) images alongside a picture of the furnace in operation. The furnace's body, fully displayed in Fig. 1(*a*), was 3D printed using direct metal laser sintering and made of stainless steel. Such an additive manufacturing technique enables cost-effective replication and customization of the design to accommodate various beamline requirements. The furnace body is fully water cooled to maintain a temperature near ambient conditions. This acts as a safety measure in the event of skin contact with the furnace's exterior and helps ensure spatial positioning accuracy by reducing the risk of thermal drift.

To minimize unwanted turbulence and enhance thermal efficiency, the furnace features several printed fixed screens with maximum openings. These are supplemented by laser-cut stainless steel sheets that slide in, serving as radiation shields to reduce openings and decrease air turbulence at the sample position. This design facilitates easy adaptation for various measurements using the same furnace body and simplifies maintenance, as the laser-cut thin metal sheets can be easily replaced.

The furnace body has a small aperture for the incident X-ray beam and a larger opening on the opposite side to allow both transmitted and diffracted beams to exit. This wider

aperture supports diffraction angles up to ±50°, enabling a broad 2θ range. To maintain X-ray transparency while minimizing air turbulence, the exit opening is sealed with a removable Kapton sheet [see Fig. 1(*b*)]. This sheet is air cooled to prevent melting. The furnace also includes two side openings that can be used for X-ray fluorescence measurements, thermal imaging, laser probing or inert gas inflow, demonstrating the system's versatility. During DFXM experiments, these side holes can be easily sealed with stainless steel covers that are highly reflective to infrared radiation.

Five slots are available for inserting heater elements, which enter the furnace from the top and surround the sample, as illustrated in the bottom view of Fig. 1(*a*). The upper part of each heater element remains in contact with the water-cooled furnace body. This design is necessary to keep the connectors at a low temperature, though it does result in some energy loss. The five slots may all be used or not, depending on the required X-ray geometry. For DFXM measurement, a set of four resistances has been inserted inside the furnace. These resistances are made of silicon nitride and have the reference number 82306B. They can be provided by various manufacturers. A *K*-type thermocouple is used to monitor the internal temperature and adjust the heating power to follow the setpoint using a PID temperature controller. This thermocouple is typically positioned a few millimetres above the sample to avoid any unintended collision with it. The thermocouple and heater elements are secured in place using ceramic cement (Resbond 940, Cotronics).

For safety, the power supply to the heater elements is interlocked with both a water-flow meter, monitoring the water outflow from the furnace body, and an air-flow meter, ensuring the cooling of the Kapton window. Should either of these two cooling systems fail, the power supply is automatically cut off.

2.2. Integration to the ID03 beamline

Two motorized stages allow for precise translation of the furnace along the *y* (horizontal, perpendicular to the beam) and *z* (vertical) directions, while manual adjustment along the *x* axis (parallel to the X-ray beam) is achieved using a lead screw and guided rails. A reference marker on the rail facilitates reproducible positioning along *x*. Once the furnace and sample are aligned in the *x*–*y* plane, the furnace can be translated vertically (*z*) to move it out of the beam path without disturbing the sample's alignment. The furnace is mounted on a separate granite gantry, independent of the sample goniometer. This design ensures that any vibrations related to furnace operation, such as those caused by air or water flow, do not transfer to the sample.

The motion of the furnace and the sample are fully decoupled. This design permits sample rotations about the vertical axis (ω angle) as well as tilts about the horizontal axes (μ and χ angles, see Fig. 1 for the definition of the angles). The current setup allows for rotational flexibility of up to ±25° about μ and χ, and full 360° rotation about ω, which is critical for orienting single grains or domains during diffraction imaging experiments and also for tomography measurements. The available translation space exceeds 2 mm, which is sufficient for spatial scans across the sample surface or depth profiling.

The design also accommodates a near-field imaging camera (Isern *et al.*, 2025), a high-resolution detector system based on a PCO sensor coupled with visible-light optics, yielding an effective pixel size of ∼0.65 µm. This detector can be positioned as close as 50 mm to the sample, even with the furnace in place, due to the compact geometry and top-mounted cabling. The cabling layout ensures that neither the rotational freedom of the goniometer nor the translational motion of the furnace are obstructed. This near-field detector is essential to the measurements performed at the beamline as it is generally used for sample positioning, grain alignment, phase-contrast tomography and high-resolution rocking curves of a part of the diffraction ring (Ahl *et al.*, 2020; Lee *et al.*, 2024).

Finally, the furnace system is integrated with the beamline control software and can be operated remotely via a dedicated *BLISS* session (https://gitlab.esrf.fr/bliss/bliss; https://www.esrf.fr/BLISS), eliminating the need to enter the experimental

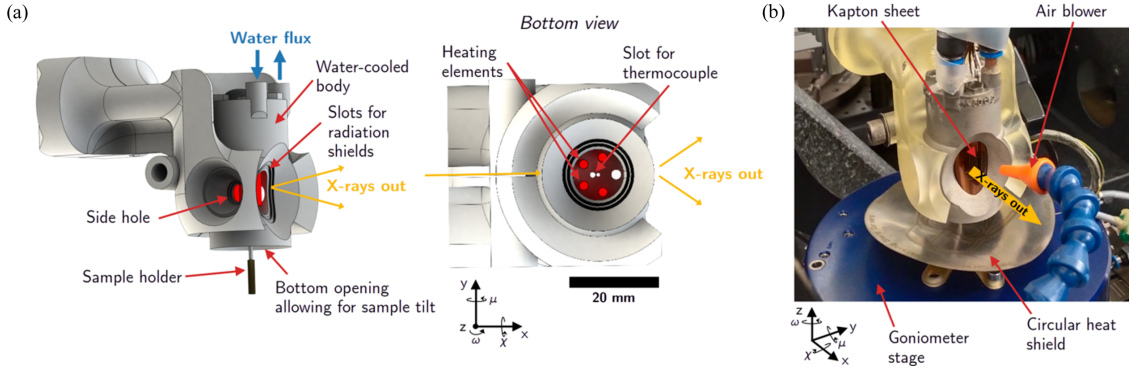

Figure 1
Design and integration of the *in situ* furnace for synchrotron experiments. (*a*) CAD rendering showing a side and bottom view of the furnace, with the laboratory coordinate system overlaid in black: *x* is along the incident X-ray beam direction and *z* is vertical. Key components such as the sample holder slots, X-ray beam aperture and water-cooling channels are visible. The bottom view shows the placement of the thermocouple and resistive heaters, between which the sample is inserted. (*b*) Photograph of the furnace mounted on the beamline goniometer. A circular heat shield is inserted on the bottom part to protect the goniometer. The angles μ, χ and ω represent goniometer rotations about the laboratory coordinate axes.

hutch during alignment or temperature ramping. This facilitates efficient and safe operation, especially during long-duration or high-temperature experiments.

This modular and flexible integration makes the system suitable for a wide range of *in situ* synchrotron experiments, including thermally activated deformation, phase transitions, and recovery studies using advanced diffraction imaging techniques.

2.3. Temperature distribution within the furnace

To verify the temperature homogeneity inside the furnace, a K-type thermocouple was positioned in place of the sample, allowing it to be moved using the sample's goniometer motors along the laboratory x, y and z axes. These temperature measurements are displayed in Fig. 2. Initially, the thermocouple was placed at the origin ($x = y = z = 0$) to align the beam, the inbound and outbound X-ray apertures, and the thermocouple. The initial x position was chosen to be sufficiently distant from the resistances, allowing the sample to be tilted. The y and z origin positions were chosen to align the beam and the tip of the thermocouple.

Measurements were conducted for temperatures ranging from 400 to 1000°C, as detailed in Table 1, along with the power required to maintain these temperatures. As a test, a peak temperature of 1200°C was achieved with a heating power of 350 W. However, this resulted in the failure of one heater element after a few minutes, which in turn caused the failure of the other elements. Since a temperature of 1000°C could be maintained continuously for 100 h, we established this as the maximum tested operating temperature with minimal risk of damaging the heater elements. During these heating cycles, an additional thermocouple was positioned on the goniometer stage, recording a maximum temperature of 27°C. This confirms that the furnace transmits negligible heat to the other components of the beamline setup.

Table 1
Target temperatures and corresponding delivered power.

Target temperature (°C)	400	600	800	1000
Delivered power (W)	65	95	130	215

The results show that for each target temperature, within a region of ±1 mm, the temperature difference relative to the origin position remains below 20°C along the x axis, and 60°C along the y and z axes. This level of variation is expected to have minimal impact on temperature homogeneity, particularly in metallic samples commonly studied with DFXM, due to their high thermal conductivity, which promotes uniform temperature distribution. Additionally, given that the typical field of view in DFXM experiments is ∼100 µm, it is reasonable to assume that the grain of interest experiences a nearly uniform temperature throughout.

Fig. 3, steps 1 to 5, shows the heating and cooling rates in a standard operation mode, that is, for a ramp rate set to 1000°C min^{-1}. It shows that the various targeted temperature plateaus (200, 400 and 800°C in steps 1, 2 and 3, respectively) were achieved with the targeted ramp rate. Once the target is reached, the temperature stabilizes with variations of less than ±2°C. Steps 4 and 5 show a stepwise cooling rate to 600°C and further to room temperature. The cooling process relies on natural convection upon turning off the heater elements or removing the furnace by translating it in the vertical direction. While the furnace was tested here without any active cooling system, its side apertures can accommodate a gas inflow to enhance the cooling rate.

The time evolution of the furnace temperature was fitted using an exponential decay model, as in equation (1),

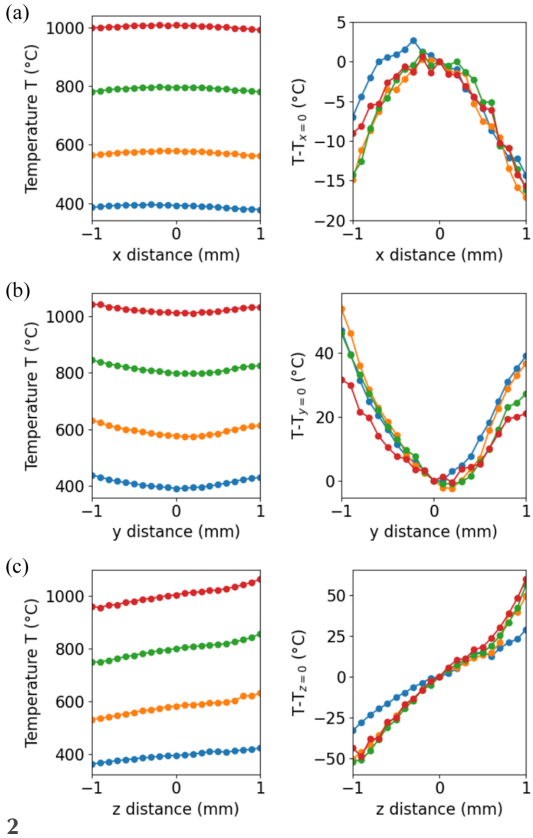

Figure 2
Temperature as a function of the position of the thermocouple sample in the furnace along (*a*) the x axis, (*b*) the y axis and (*c*) the z axis. Left panels show the absolute temperature; right panels show the temperature difference relative to the origin position ($x = y = z = 0$). Blue, orange, green and red curves correspond to set temperatures of 400, 600, 800 and 1000°C, respectively.

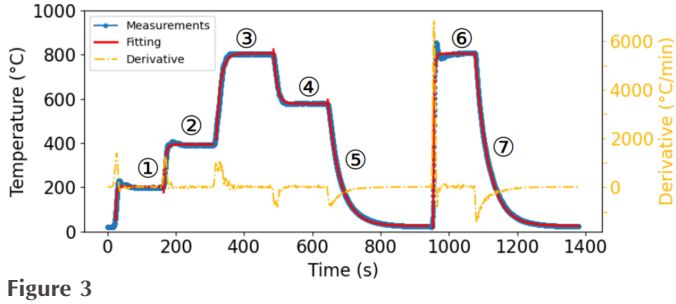

Figure 3
Heating and cooling ramp rates for given temperature setpoints. Red curves refer to fitted curves following equation (1), for which the fitting parameters are available in Table 2. The yellow curve shows the derivative of the fitted heating and cooling curve.

Table 2
Fit parameters for equation (1) to characterize the temperature ramp using a K-type thermocouple.

For steps 4 to 7, no ramp rate was set in order to evaluate the maximum heating and cooling rates of the furnace.

Temperature step	Set ramp rate (°C min^{-1})	A (°C)	τ (s)
1	100	-153 ± 9	2.34 ± 0.20
2	100	-217 ± 5	5.11 ± 0.16
3	100	-391 ± 4	12.60 ± 0.23
4	Max.	246 ± 2	10.34 ± 0.15
5	Max.	570 ± 1	37.05 ± 0.11
6	Max.	-789 ± 24	2.96 ± 0.14
7	Max.	779.55 ± 2	39.04 ± 0.14

$$T(t) = T_0 + A \exp\left(-\frac{t}{\tau}\right). \quad (1)$$

The fitting parameters are available in Table 2. To further characterize the capabilities of the furnace, step 6 consisted of heating the furnace as quickly as possible to 800°C without a fixed ramp rate, while step 7 involved the subsequent cooling to room temperature. This operation revealed that the furnace can achieve a heating rate above 6000°C min^{-1}. However, such a fast ramp rate tends to induce a temperature overshoot, which could be critical for some applications. Adjusting the PID parameters of the furnace may mitigate this overshoot, but would result in a decrease in the ramp rate close to the setpoint.

3. Results

3.1. Temperature characterization from the lattice parameter evolution of iron

The temperature of the sample, T_{sample}, can differ from the temperature measured by the furnace control thermocouple, T_{furnace}, which regulates the heating setpoint. Since the thermocouple is positioned a few millimetres above the sample rather than directly on it, thermal gradients and delayed thermal response can occur. Furthermore, the sample temperature depends on its absorption of electromagnetic waves, primarily infrared radiation, emitted by the furnace resistances, and thus varies with the material properties of the sample. These factors can lead to inaccurate estimates of the actual sample temperature. Such discrepancies are particularly critical in temperature-sensitive studies, such as phase transformations, where precise temperature measurement is essential.

To directly determine T_{sample}, we employed *in situ* X-ray diffraction to track the evolution of the lattice parameter of iron in its ferritic phase during heating on an area detector. In addition, iron undergoes a well known phase transformation from body-centered cubic (b.c.c.) α-ferrite to face-centered cubic (f.c.c.) γ-austenite at 912°C at ambient pressure. This transformation is accompanied by abrupt changes in lattice symmetry and spacing, making it an ideal reference point for temperature calibration. We exploited this transformation as an internal thermometer to calibrate the sample temperature independently of the furnace readout.

The sample, a 1 mm-thick square cross-section bar of commercially pure iron, was heated at a rate of 100°C min^{-1}. Diffraction patterns were recorded every 5 s using a FReLoN CCD detector with a resolution of 2048 × 2048 pixels and a pixel size of 47.3 µm, positioned 282 mm downstream of the sample (Isern *et al.*, 2025). The X-ray beam was monochromatic with an energy of 55.12 keV, selected using a silicon (111) channel-cut monochromator. This high energy allowed simultaneous probing of several diffraction peaks from both the b.c.c. and f.c.c. phases over a broad angular range.

The 2D diffraction images displayed concentric Debye–Scherrer rings, characteristic of polycrystalline materials with randomly oriented grains. These rings were azimuthally integrated over 360° using the Python library *pyFAI* (Kieffer *et al.*, 2020; Ashiotis *et al.*, 2015) to produce 1D diffractograms of intensity versus scattering angle. The detector geometry was calibrated using standard polycrystalline silicon powder. The resulting integrated patterns reveal the evolution of the diffraction peaks during heating.

Fig. 4(*a*) shows representative diffractograms before and after the $\alpha \rightarrow \gamma$ transformation, alongside the corresponding 2D diffraction images. The smaller peaks that are not indexed are attributed to surface oxides. During heating, the b.c.c. peaks shift continuously due to thermal expansion, while new f.c.c. peaks appear abruptly upon transformation. Red arrows mark the emergence of these austenitic reflections, providing a clear signature for identifying the transformation point.

To estimate T_{sample} during the heating ramp, we extracted the lattice parameter a of b.c.c. iron from the Bragg peak positions corresponding to the (110), (200) and (211) reflections, using Bragg's law. Assuming the lattice expands linearly with temperature in the α phase, and that its value is known at room temperature and at the $\alpha \rightarrow \gamma$ transformation point (912°C), we applied a linear interpolation. Fig. 4(*b*) illustrates this relationship between T_{sample} and the lattice parameter of α-iron. This yields an effective thermal-expansion coefficient of $\alpha_L = 16 \times 10^{-6}$°C^{-1}, consistent with literature values for ferritic iron (Nix & MacNair, 1941).

Fig. 4(*c*) compares the interpolated T_{sample} with the furnace setpoint T_{furnace}. A clear linear relationship is observed between the two; as plotted in green, the difference $T_{\text{furnace}} - T_{\text{sample}}$ steadily increases with T_{furnace}, with a slightly faster increase for low temperatures (<300°C). This correlation enables a practical offset calibration. For a given sample, the exact relationship depends on sample positioning and furnace geometry; this approach should be reliable considering the temperature profile along laboratory translation axes shown in Fig. 2. To assess stability and reproducibility, we repeated the heating and cooling cycles multiple times. In all cases, the onset of the $\alpha \rightarrow \gamma$ transformation during heating and the reverse transformation during cooling occurred within ±5°C of the previously determined transition temperature. This consistency confirms the reliability of both the furnace system and the diffraction-based temperature calibration. Because the relationship shown in Fig. 4(*c*) depends on the material's

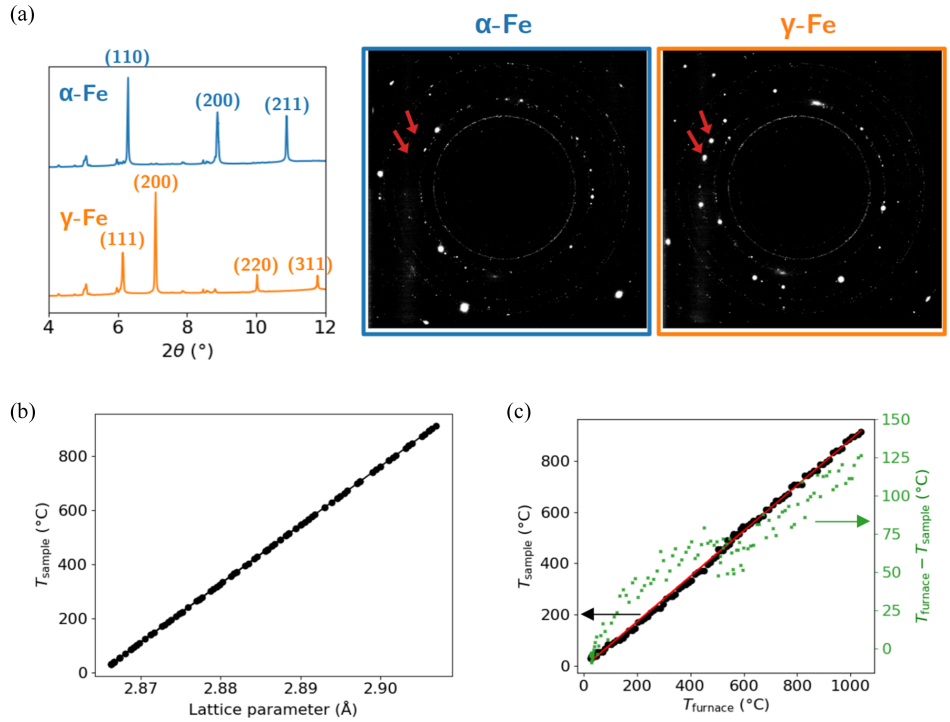

Figure 4
Temperature calibration of the sample through lattice parameter evolution and austeno-ferritic transformation of iron. (*a*) Integrated 1D diffractograms and detector images for the iron sample before and after the α-iron to γ-iron transition. Red arrows indicate the easily identifiable diffraction spots related to the (200) reflection of austenite, which are not visible in the ferritic state. (*b*) Evolution of the sample temperature determined from the lattice parameter evolution of α-iron. (*c*) Sample temperature and furnace–sample temperature difference as a function of furnace temperature.

absorption properties, and therefore on its nature, it is recommended to perform this calibration prior to any experiment.

In summary, this method offers a robust and material-intrinsic way to determine the true temperature of a sample for *in situ* synchrotron experiments. By utilizing a well known phase transformation and tracking lattice parameter evolution with high precision, we provide a reliable internal thermometer. This correction enables more accurate interpretation of structural changes and can be extended to other materials with sharp transformation points.

3.2. DFXM monitoring of strain relaxation and grain growth in aluminium 1050 alloy

As a demonstration of the *in situ* capabilities of the system, we present a study of local orientation changes and grain growth in a 50% cold-rolled f.c.c. aluminium 1050 (Al1050) sample during annealing. The specimen, with a cross section of 500 µm × 500 µm and a height of 5 mm, was glued to a ceramic stick using heat-resistant adhesive (Aron Ceramic E) and mounted on the ID03 goniometer. A parallel X-ray beam of size 600 µm × 600 µm was used to illuminate the grain, enabling a 2D projection scan of the local orientation by tilting the sample about the x and y axes (χ and μ tilts). This grain was selected from those that satisfied the diffraction conditions within the sample's χ and μ tilt range and produced a diffracted beam oriented towards the far-field detector. The grain producing the most intense diffracted beam was chosen, as this intensity indicates a large grain size, thereby facilitating the observation of any changes upon annealing.

The diffracted X-rays from the (200) reflection were magnified using an objective composed of 87 beryllium compound refractive lenses with a 50 µm radius, positioned 260 mm from the sample. The signal was projected onto a far-field detector located 5346 mm downstream using an indirect detection system comprising a scintillator screen, a 2× visible-light objective and a PCO.edge camera, yielding an effective pixel size of 175 nm.

The furnace was positioned around the sample using the near-field camera to ensure the X-ray beam was centered within the inbound X-ray aperture. A grain of the as-received sample was scanned using DFXM prior to the furnace temperature ramp, which was performed stepwise at a rate of 100°C min^{-1}. During heating, the grain's lattice parameter increased, reducing the 2θ angle. To track the grain, the objective was removed, and the diffraction spot was followed by incrementally lowering the far-field detector. Periodically, the temperature was stabilized, the objective reinserted, and its pitch angle (2θ angle) and z position realigned to ensure the diffracted beam passed through, allowing verification of the grain's real-space image. Using the 2θ angle of the (200) reflection and the thermal-expansion coefficient of aluminium from the literature (Wilson, 1941), the lattice parameter, and thus the actual sample temperature, was determined. The maximum temperature reached was 630°C, held for 1 min,

after which visible changes in grain morphology were observed. The furnace was then cooled, and the same grain was rescanned under the initial conditions.

Fig. 5(*a*) presents orientation maps of the sample in its as-received and annealed states, generated from DFXM image stacks after standard preprocessing steps, including background subtraction, region-of-interest selection and hot pixel removal. Additional details on the data-analysis workflow are provided by Garriga Ferrer *et al.* (2023). The sample position and tilt range remained nearly identical between the two measurements, ensuring that the same grain was tracked before and after annealing. This is further supported by the identifiable features (indicated by arrows) that persist across both states.

Before annealing, the grain exhibits a clear orientation gradient and heterogeneous internal structure. Following heat treatment, the grain interior becomes significantly more homogeneous, suggesting a reduction in internal mosaicity. This transformation is consistent with a decrease in dislocation density and enhanced recovery processes. This observation is quantitatively supported by Fig. 5(*b*), which illustrates the distribution of local orientation differences across all pixels of the map. For each pixel, the local orientation difference is calculated as $\Delta\theta = (\Delta\mu^2 + \Delta\chi^2)^{1/2}$ (Ahl *et al.*, 2017), where $\Delta\mu$ and $\Delta\chi$ represent the average orientation difference with the eight neighboring pixels. Following annealing, the distribution shifts toward lower $\Delta\theta$ values, confirming a significant reduction in intragranular misorientation and a more uniform internal orientation field.

The grain also expanded during annealing. The projected grain area, A, calculated by multiplying the number of contributing pixels by the effective pixel area (175 nm × 175 nm), increased from $A = 21 \times 10^3$ to $A = 27 \times 10^3$ µm, corresponding to ∼30% growth. This growth, alongside the reduction in internal orientation spread, results in a stronger signal-to-noise ratio compared with the pre-annealed state, yielding neater edges for the post-annealing grain. While this measurement captures the 2D projected area and does not provide volumetric data, it clearly indicates grain growth driven by grain-boundary migration during annealing. The grain growth observed during annealing appears to be rather directional; the expansion is not isotropic, suggesting that different grain boundaries exhibited varying mobilities. This variation in boundary motion likely reflects differences in boundary character and local driving forces, leading to uneven growth along different interfaces.

Overall, this example demonstrates the capabilities of the furnace setup for *in situ* heat treatment studies using DFXM. The ability to perform annealing without dismounting the sample, while retaining full flexibility in motion and rotation, highlights the system's effectiveness for tracking microstructural evolution under well controlled thermal conditions.

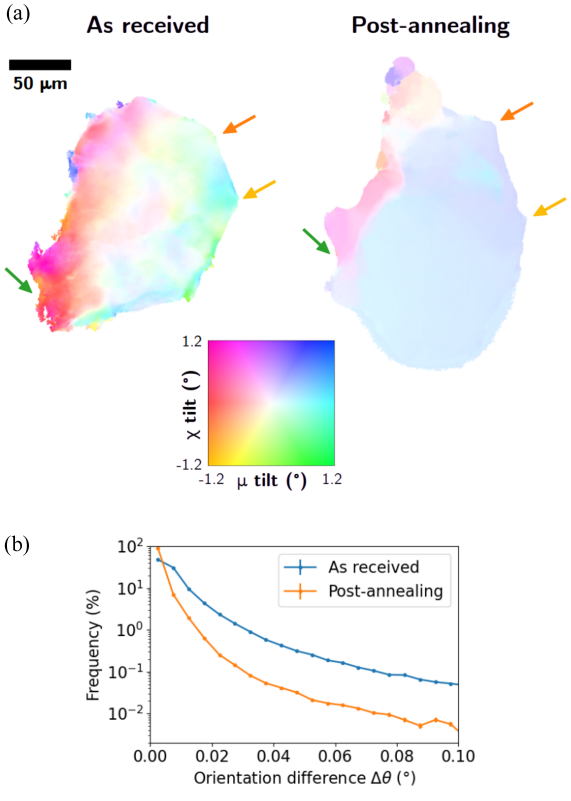

Figure 5
Effect of annealing on the misorientation within a grain. (*a*) Mosaicity map of a grain from a 50% cold-rolled Al1050 sample before and after annealing. Arrows indicate distinguishable common features of the grain before and after growth. (*b*) Frequency of the orientation difference across all pixels of the grain, pre- and post-annealing.

4. Conclusions

We have demonstrated a non-contact radiation furnace developed for versatile X-ray measurement and commissioned for *in situ* high-temperature X-ray studies at the ID03 beamline of ESRF. The furnace was calibrated up to 1000°C using two independent approaches: direct thermocouple measurements for temperature mapping and ramp-rate assessment, and synchrotron diffraction tracking of the ferrite-to-austenite transformation in iron. These methods confirm thermal stability and reproducibility suitable for precise crystallographic experiments. With heating rates exceeding 6000°C min^{-1} and potential operation above 1000°C, the system is well suited for studies on metallic alloys, ceramics and functional materials. Though optimized for DFXM, the furnace is fully compatible with additional techniques such as 3DXRD, topotomography and phase-contrast tomography; it could also be readily adapted to other beamlines. A first application on cold-rolled Al1050 demonstrated the system's capability to resolve strain evolution during annealing.

Current limitations include the inability to perform rapid quenching or apply mechanical strain during heating. The furnace also lacks a fully sealed atmosphere; while flowing inert gas can mitigate oxidation, strongly oxidizing materials should be enclosed in sealed capillaries. Despite these constraints, the system offers significant flexibility and precision for thermal studies of microstructural evolution across a wide range of synchrotron applications.

Acknowledgements

We thank ESRF for providing the beam time at ID03.

Conflict of interest

The authors declare that there are no conflicts of interest.

Data availability

Raw data were generated at the ESRF large-scale facility. Derived data supporting the findings of this study are available from the corresponding author upon reasonable request.

Funding information

CY, AS, VS and LL acknowledge the financial support from the ERC Starting Grant No. 10116911.

References

Ahl, S., Simons, H., Detlefs, C., Jensen, D. J. & Poulsen, H. (2020). *Acta Mater.* **185**, 142–148.
Ahl, S. R., Simons, H., Zhang, Y., Detlefs, C., Stöhr, F., Jakobsen, A. C., Juul Jensen, D. & Poulsen, H. F. (2017). *Scr. Mater.* **139**, 87–91.
Ashiotis, G., Deschildre, A., Nawaz, Z., Wright, J. P., Karkoulis, D., Picca, F. E. & Kieffer, J. (2015). *J. Appl. Cryst.* **48**, 510–519.
Bellet, D., Gorges, B., Dallery, A., Bernard, P., Pereiro, E. & Baruchel, J. (2003). *J. Appl. Cryst.* **36**, 366–367.
Buras, B., Lebech, B. & Kofoed, W. (1984). *Rev. Phys. Appl. (Paris)* **19**, 743–745.
Cloetens, P., Daillant, J., Detlefs, C., Drnec, J., Frey, J., Hernandez, J.-A., Honkimaki, V., Krisch, M., Martínez-Criado, G., McCarthy, J., Mezouar, M., Di Michiel, M., Mitchell, E., Pacureanu, A., Qin, Q., de Sanctis, D., Sette, F., Tafforeau, P., Torchio, R., Watier, Y., Wright, J. & Yildirim, C. (2025). *Synchrotron Radiat. News* **38**(1), 4–9.
Cloetens, P., Pateyron-Salomé, M., Buffière, J.-Y., Peix, G., Baruchel, J., Peyrin, F. & Schlenker, M. (1997). *J. Appl. Phys.* **81**, 5878–5886.
Derome, D., Griffa, M., Koebel, M. & Carmeliet, J. (2011). *J. Struct. Biol.* **173**, 180–190.
Dresselhaus-Marais, L. E., Winther, G., Howard, M., Gonzalez, A., Breckling, S. R., Yildirim, C., Cook, P. K., Kutsal, M., Simons, H., Detlefs, C., Eggert, J. H. & Poulsen, H. F. (2021). *Sci. Adv.* **7**, eabe8311.
Fife, J. L., Rappaz, M., Pistone, M., Celcer, T., Mikuljan, G. & Stampanoni, M. (2012). *J. Synchrotron Rad.* **19**, 352–358.
Garriga Ferrer, J., Rodríguez-Lamas, R., Payno, H., De Nolf, W., Cook, P., Solé Jover, V. A., Yildirim, C. & Detlefs, C. (2023). *J. Synchrotron Rad.* **30**, 527–537.
Hirao, N., Kawaguchi, S. I., Hirose, K., Shimizu, K., Ohtani, E. & Ohishi, Y. (2020). *Matter Radiat. Extremes* **5**, 018403.
Holler, M., Aidukas, T., Heller, L., Appel, C., Phillips, N. W., Müller-Gubler, E., Guizar-Sicairos, M., Raabe, J. & Ihli, J. (2022). *J. Synchrotron Rad.* **29**, 1223–1231.
Isern, H., Brochard, T., Dufrane, T., Brumund, P., Papillon, E., Scortani, D., Hino, R., Yildirim, C., Rodriguez Lamas, R., Li, Y., Sarkis, M. & Detlefs, C. (2025). *J. Phys. Conf. Ser.* **3010**, 012163.
Kieffer, J., Valls, V., Blanc, N. & Hennig, C. (2020). *J. Synchrotron Rad.* **27**, 558–566.
Kutsal, M., Bernard, P., Berruyer, G., Cook, P., Hino, R., Jakobsen, A., Ludwig, W., Ormstrup, J., Roth, T., Simons, H., Smets, K., Sierra, J. X., Wade, J., Wattecamps, P., Yildirim, C., Poulsen, H. F. & Detlefs, C. (2019). *IOP Conf. Ser. Mater. Sci. Eng.* **580**, 012007.
Lang, A. R. (1993). *J. Phys. D Appl. Phys.* **26**, A1–A8.
Lee, S., Berman, T. D., Yildirim, C., Detlefs, C., Allison, J. E. & Bucsek, A. (2024). *Sci. Rep.* **14**, 6241.
Martínez-Criado, G., Steinmann, R., Alén, B., Labrador, A., Fuster, D., Ripalda, J. M., Homs, A., Labouré, S. & Susini, J. (2007). *Rev. Sci. Instrum.* **78**, 025106.
Mavrikakis, N., Detlefs, C., Cook, P., Kutsal, M., Campos, A., Gauvin, M., Calvillo, P., Saikaly, W., Hubert, R., Poulsen, H. F., Vaugeois, A., Zapolsky, H., Mangelinck, D., Dumont, M. & Yildirim, C. (2019). *Acta Mater.* **174**, 92–104.
Mitchell, E. P. & Garman, E. F. (1994). *J. Appl. Cryst.* **27**, 1070–1074.
Nix, F. & MacNair, D. (1941). *Phys. Rev.* **60**, 597–605.
Nopens, M., Greving, I., Flenner, S., Hesse, L., Lüdtke, J., Altgen, M., Koch, G., Beruda, J., Heldner, S., Köhm, H., Kaschuro, S., Olbrich, A., Mietner, J. B., Scheckenbach, F., Sieburg-Rockel, J. & Krause, A. (2025). *J. Synchrotron Rad.* **32**, 1354–1360.
Poulsen, H. F. (2004). *Three-dimensional X-ray diffraction microscopy: mapping polycrystals and their dynamics*, Vol. 205 of *Springer Tracts in Modern Physics.* Springer Science & Business Media.
Puig-Molina, A., Gorges, B. & Graafsma, H. (2001). *J. Appl. Cryst.* **34**, 677–678.
Reischig, P., King, A., Nervo, L., Viganó, N., Guilhem, Y., Palenstijn, W. J., Batenburg, K. J., Preuss, M. & Ludwig, W. (2013). *J. Appl. Cryst.* **46**, 297–311.
Simons, H., King, A., Ludwig, W., Detlefs, C., Pantleon, W., Schmidt, S., Stöhr, F., Snigireva, I., Snigirev, A. & Poulsen, H. F. (2015). *Nat. Commun.* **6**, 6098.
Snell, E. H., Bellamy, H. D., Rosenbaum, G. & van der Woerd, M. J. (2007). *J. Synchrotron Rad.* **14**, 109–115.
Van Rijn, R., Ackermann, M. D., Balmes, O., Dufrane, T., Geluk, A., Gonzalez, H., Isern, H., de Kuyper, E., Petit, L., Sole, V. A., Wermeille, D., Felici, R. & Frenken, J. W. M. (2010). *Rev. Sci. Instrum.* **81**, 014101.
Wilson, A. (1941). *Proc. Phys. Soc.* **53**, 235–244.
Yildirim, C., Ballet, P., Santailler, J.-L., Giotta, D., Obrecht, R., Tran Thi, T. N., Baruchel, J. & Brellier, D. (2021). *J. Synchrotron Rad.* **28**, 301–308.
Yildirim, C., Cook, P., Detlefs, C., Simons, H. & Poulsen, H. F. (2020*a*). *MRS Bull.* **45**, 277–282.
Yildirim, C., Mavrikakis, N., Cook, P., Rodriguez-Lamas, R., Kutsal, M., Poulsen, H. & Detlefs, C. (2022). *Scr. Mater.* **214**, 114689.
Yildirim, C., Shukla, A., Zhang, Y., Mavrikakis, N., Lesage, L., Sanna, V., Sarkis, M., Li, Y., La Bella, M., Detlefs, C. & Poulsen, H. F. (2025). *Commun. Mater.* **6**, 198.
Yildirim, C., Vitoux, H., Dresselhaus-Marais, L. E., Steinmann, R., Watier, Y., Cook, P. K., Kutsal, M. & Detlefs, C. (2020*b*). *Rev. Sci. Instrum.* **91**, 065109.